Delft University of Technology

Image scanning microscopy
a vectorial physical optics analysis

Hung, S.; Kalisvaart, Dylan; Smith, Carlas

Important note
To cite this publication, please use the final published version (if applicable).
Please check the document version above.

Image scanning microscopy: a vectorial physical optics analysis

SHIH-TE HUNG,[1,3] **DYLAN KALISVAART,**[1]   **AND CARLAS SMITH**[1,2,4]

[1]*Delft Center for Systems and Control, Delft University of Technology, Delft, The Netherlands*
[2]*Department of Imaging Physics, Delft University of Technology, Delft, The Netherlands*
[3]*s.hung-1@tudelft.nl*
[4]*C.S.Smith@tudelft.nl*

Abstract: Image scanning microscopy (ISM) achieves resolution beyond the diffraction limit by a factor of $\sqrt{2}$. However, prior ISM research predominantly employs scalar diffraction theory, neglecting critical physical effects such as polarization, aberrations, and Stokes shift. This paper presents a comprehensive vectorial ISM point spread function (PSF) model that accounts for these phenomena. By considering the effect of polarization in emission and excitation paths, as well as aberrations and Stokes shift, our model provides a more accurate representation of ISM. We analyze the differences between scalar and vectorial theories in ISM and investigate the impact of pinhole size and aberration strength on resolution. At a numerical aperture of 1.2, the full width half maximum (FWHM) discrepancy between scalar and vectorial ISM PSFs can reach 45 nm, representing a 30% deviation from the vectorial model. Additionally, we explore multiphoton excitation in ISM and observe increased FWHM for 2-photon and 3-photon excitation compared to 1-photon excitation. The FWHM of the 2-photon excitation ISM PSF increases by 20% and the FWHM of the 3-photon excitation ISM PSF increases by 28% compared to the 1-photon excitation ISM. In addition, we found that the optimal sweep factor for 2-photon ISM is 1.22, and the optimal sweep factor of 3-photon ISM is 1.12 instead of the 2 predicted by the one-photon scalar ISM theory. Our work improves the understanding of ISM and contributes to its advancement as a high-resolution imaging technique.

1. Introduction

Fluorescence microscopy is a powerful tool for bioimaging, as fluorescent labeling enables high imaging specificity and contrast. However, the resolution of conventional fluorescence microscopy cannot surpass the diffraction limit [1]. To circumvent this limit, several super-resolution technologies have been developed. Stimulated emission depletion microscopy (STED) combines a confocal spot to create fluorescence with a donut to deplete the fluorescence at the edge of the confocal spot. This synergetic combination reduces the effective width of the confocal spot and thereby surpasses the diffraction limit [2,3]. Single-molecule localization microscopy (SMLM) surpasses the diffraction limit by localizing sparsely activated single-molecules [4–6]. Structured illumination microscopy (SIM) adopts in-plane sinusoidal illumination to expand the effective bandwidth of spatial frequencies to enhance the resolution [7,8].

SIM is the preferred super-resolution method for live-cell imaging because of the low illumination intensity, the flexibility in the choice of fluorophores or dyes, and the imaging speed. Although the original approaches relied on complex hardware and post-processing, in recent years we have seen a steady rise of less involved approaches that fundamentally make use of the same principles, such as image scanning microscopy [9]. ISM relies on the shifts between excitation and emission point spread function to create a sharper PSF with better imaging

resolution. Several microscopes have been developed based on this principle [10–12]. The first implementation of ISM was based on confocal microscopy with a camera detector, where pixels were re-assigned in post-processing to create a super-resolution reconstruction [12]. Re-scan confocal microscopy performs this computation optically by adopting a second galvo mirror, which moves at a different speed to perform this shift operation [11]. Optical photon reassignment microscopy (OPRA) achieved ISM with only a single galvo mirror, which is used twice [10]. The speed of these ISM approaches is similar to confocal microscopy and multiplexing the number of illumination spots can increase the imaging speed [13,14].

A robust theoretical foundation is essential for the evaluation and advancement of existing and innovative approaches in the field of illumination scanning microscopy (ISM). In the context of high-numerical aperture (NA) fluorescence microscopy, the Stokes shift of fluorescence represents a ubiquitous phenomenon across various fluorescent dyes. Furthermore, even cutting-edge optical setups are susceptible to aberrations, while the presence of polarization effects is inherent within the microscopy system. As such, these factors demand careful consideration when modeling the point spread function (PSF) [15]. Notably, the significance of polarization effects on PSF modeling is particularly pronounced in high-NA systems [16], and the precision of vectorial PSF modeling has been experimentally validated [15,17]. While prior ISM researches have contributed to scalar aberration-free PSF modeling [11,18], the Stokes shift effect [19], vectorial effects for PSF-engineered ISM [20], and multiphoton excitation ISM [21–24], a comprehensive vectorial ISM PSF modeling methodology, accounting for all the aforementioned effects, remains an unmet need. The availability of a reliable ISM PSF simulator offers a valuable reference for assessing the quality of ISM images and for selecting optimal optical elements and hardware parameters for ISM microscopy.

In this research, we develop this vectorial ISM PSF model considering the effects of polarization, Stoke shift, and aberrations. We investigate the predicted resolution improvement for single- and multiphoton excitation using the scalar and vectorial models. This is done by analyzing the differences of these models over the whole range of possible NA. We find that the highest resolution improvement can be achieved with 1-photon excitation and that the difference between the scalar and vectorial models increases with the NA. We investigate if the resolution improvement is robust against aberrations and how this can be mitigated. We find that aberrations decrease the resolution and that the effect of aberrations can be reduced by decreasing the size of the pinhole.

2. Theory

2.1. Scalar theory of image scanning microscopy PSF

The scalar theory of ISM PSF was previously developed independently in two works [11,18]. In this subsection, we expand upon the scalar theory of ISM from [11] by incorporating vectorial effects, Stokes shift, and aberrations. The ISM PSF equation can be described as follows [11]:

$$
\begin{aligned}
\mathrm{H_{ISM}}\left(\boldsymbol{u}_\mathrm{c} - \boldsymbol{u}_\mathrm{o}, u_\mathrm{z}\right) = M^2 \\
\int d^2 u_\mathrm{s} D\left(M\left(\boldsymbol{u}_\mathrm{s} - \boldsymbol{u}_\mathrm{c}\right)\right) \mathrm{H_{em}}\left(M\left(\boldsymbol{u}_\mathrm{c} - \boldsymbol{u}_\mathrm{s}\right) - \boldsymbol{u}_\mathrm{s} - \boldsymbol{u}_\mathrm{o}, -u_\mathrm{z}\right) \mathrm{H_{ex}}\left(\boldsymbol{u}_\mathrm{o} - \boldsymbol{u}_\mathrm{s}, u_\mathrm{z}\right),
\end{aligned}
\tag{1}
$$

where $\mathrm{H_{ISM}}(\boldsymbol{u}, u_z), \mathrm{H_{em}}(\boldsymbol{u}, u_z), \mathrm{H_{ex}}(\boldsymbol{u}, u_z)$ are the two-dimensional PSFs of an image scanning microscope, emission, and excitation of the widefield microscope, respectively. $D(\cdot)$ is the pinhole function which is defined as a two-dimensional binary circular mask function taking value 1 inside the circle and value 0 otherwise, and M is the sweep factor for ISM which represents the scaling of shift between excitation and emission PSF [11]. Furthermore, $\boldsymbol{u}_\mathrm{c}$ are two-dimensional coordinates in the camera plane, $\boldsymbol{u}_\mathrm{s}$ is the two-dimensional position of the confocal illumination position, $\boldsymbol{u}_\mathrm{o}$ are the two-dimensional coordinates in the object, and u_z is the distance from the focal plane in the objective plane.

Taking the Fourier transform of the ISM PSF, we obtain the optical transfer function (OTF) $\widehat{H}_{ISM}(\boldsymbol{q})$:

$$\widehat{H}_{ISM}(\boldsymbol{q}, u_z) = \int d^2 q' \widehat{D}(\boldsymbol{q'}) \widehat{H}_{em}\left(-\frac{\boldsymbol{q}}{M} + \boldsymbol{q'}, -u_z\right) \widehat{H}_{ex}^*\left(\frac{(M-1)\boldsymbol{q}}{M} + \boldsymbol{q'}, u_z\right). \qquad (2)$$

Note that this equation is different concerning earlier literature as [11] contains a mistake. Here, $\boldsymbol{q} = \left(\boldsymbol{q}_x, \boldsymbol{q}_y\right)$ are normalized optical coordinates such that $\|\boldsymbol{q}\|_2 \leqslant 1$, $\widehat{H}_{em}(\boldsymbol{q})$ is the OTF of the emission PSF, $\widehat{H}_{ex}(\boldsymbol{q})$ is the OTF of the excitation PSF, and $\widehat{D}(\boldsymbol{q})$ is the OTF of the pinhole function.

2.1.1. Emission PSF and OTF

In the scalar PSF model, the electric field (E_{em}) of the emission PSF (H_{em}) can be calculated using the following equation:

$$E_{em}(\boldsymbol{u}, u_z) = \frac{1}{\sqrt{2\pi}} \int d^2 q \, c_{em}(\boldsymbol{q}) \exp\left(-i\mathbf{k}_{em}(\boldsymbol{q}) \cdot \boldsymbol{u}\right) \exp\left(-i k_z(\boldsymbol{q}) u_z\right),$$

$$c_{em}(\boldsymbol{q}) = \begin{cases} A_{em}(\boldsymbol{q}) \exp\left(-i\frac{2\pi W_{em}(\boldsymbol{q})}{\lambda_{em}}\right) & \text{if } \|\boldsymbol{q}\|_2 \leqslant 1, \\ 0 & \text{otherwise.} \end{cases} \qquad (3)$$

Here, $\mathbf{k}_{em}(\boldsymbol{q}) = \frac{2\pi NA}{\lambda_{em}}\left(\boldsymbol{q}_x, \boldsymbol{q}_y\right)$, $k_z = \sqrt{n_{med}^2 - NA^2 |\boldsymbol{q}|^2}$, and λ_{em} is the wavelength of emission light. $A_{em}(\cdot)$ is the amplitude correction factor for the emission PSF (see [25]), which is expressed as:

$$A_{em}(\theta) = \sqrt{\frac{n_{imm} \cos\theta_{imm}}{n_{med} \cos\theta_{med}}} \frac{1}{\sqrt{n_{med} \cos\theta_{med}}}. \qquad (4)$$

Here, n_{imm}, n_{med} are the respective refractive indices of the immersion and sample media, and $\theta_{imm}, \theta_{med}$ are the respective polar angle of light in the immersion and sample media. More details about the generalized Jones matrix are in the Supplement 1. $W_{ex}(\boldsymbol{q})$ is the two-dimensional pupil phase function that models the aberrations in the excitation path.

The emission PSF can be expressed as follows:

$$H_{em}(\boldsymbol{u}, u_z) = |E_{em}(\boldsymbol{u}, u_z)|^2. \qquad (5)$$

The OTF of the emission is obtained as follows:

$$\widehat{H}_{em}(\boldsymbol{q}, u_z) = \int d^2 u \, H_{em}(\boldsymbol{u}, u_z) \exp(i\mathbf{k}_{em}(\boldsymbol{q}) \cdot \boldsymbol{u}). \qquad (6)$$

2.1.2. Excitation PSF and OTF

The electric field of scalar excitation PSF (H_{ex}) is modeled as follows:

$$E_{ex}(\boldsymbol{u}, u_z) = \frac{1}{\sqrt{2\pi}} \int d^2 q \, c_{ex}(\boldsymbol{q}) \exp\left(-i\mathbf{k}_{ex}(\boldsymbol{q}) \cdot \boldsymbol{u}\right) \exp\left(-i k_z(\boldsymbol{q}) u_z\right),$$

$$c_{ex}(\boldsymbol{q}) = \begin{cases} A_{ex}(\boldsymbol{q}) \exp\left(-i\frac{2\pi W_{ex}(\boldsymbol{q})}{\lambda_{ex}}\right) & \text{if } \|\boldsymbol{q}\|_2 \leqslant 1, \\ 0 & \text{otherwise.} \end{cases} \qquad (7)$$

Here, $\mathbf{k}_{ex}(\boldsymbol{q}) = \frac{2\pi NA}{\lambda_{ex}}\left(\boldsymbol{q}_x, \boldsymbol{q}_y\right)$ and λ_{ex} is the excitation wavelength. A_{ex} is the amplitude correction factor for the excitation PSF, which is defined as follows:

$$A_{ex}(\theta) = \sqrt{\frac{n_{med} \cos\theta_{med}}{n_{imm} \cos\theta_{imm}}} \frac{1}{\sqrt{n_{imm} \cos\theta_{imm}}}. \qquad (8)$$

$W_{\text{ex}}(\boldsymbol{q})$ is the phase pupil function that models aberrations in the excitation path. The excitation PSF can be expressed as:

$$\text{H}_{\text{ex}}(\boldsymbol{u}, u_z) = |\text{E}_{\text{ex}}(\boldsymbol{u}, u_z)|^2. \tag{9}$$

The OTF of the excitation is obtained as follows:

$$\widehat{\text{H}}_{\text{ex}}(\boldsymbol{q}, u_z) = \int d^2u\, \text{H}_{\text{ex}}(\boldsymbol{u}, u_z) \exp(i\mathbf{k}_{\text{ex}}(\boldsymbol{q}) \cdot \boldsymbol{u}). \tag{10}$$

2.2.   Vectorial theory of image scanning microscopy PSF

Previous research successfully describes how resolution in ISM is achieved, but it neglects the vectorial effects and aberrations that arise with the use of high-NA objectives. To address this, we compute the vectorial PSFs taking into account Stokes shifts, aberrations, and polarization effects.

2.2.1.   Vectorial emission PSF

The emission light consists of three polarization directions (x, y, z), but only the light in the transversal direction (x, y) can propagate to the pupil plane. The electric field of the emission light, considering vectorial effects, can be expressed as follows:

$$\text{E}_{\text{em},lj}(\boldsymbol{u}, u_z) = \frac{1}{\sqrt{2\pi}} \int d^2q\, c_{\text{em},lj}(\boldsymbol{q}) \exp\left(-i\mathbf{k}_{\text{em}}(\boldsymbol{q}) \cdot \boldsymbol{u}\right) \exp\left(-ik_z u_z\right),$$

$$c_{\text{em},lj}(\boldsymbol{q}) = \begin{cases} A_{\text{em}}(\boldsymbol{q})\, \bar{\boldsymbol{M}}_{\text{em},lj}(\boldsymbol{q}) \exp\left(-i\frac{2\pi W_{\text{em}}(\boldsymbol{q})}{\lambda_{\text{em}}}\right) & , |\boldsymbol{q}| \leqslant 1 \\ 0 & , |\boldsymbol{q}| > 1 \end{cases}, \tag{11}$$

where $\text{E}_{\text{em},lj}(\boldsymbol{u}, u_z)$ is the electric field with l, j as the direction of polarization (the emitter polarization of j projects to the polarization of l in the pupil plane), $W_{\text{em}}(\boldsymbol{q})$ is the two-dimensional pupil phase function and $\bar{\boldsymbol{M}}_{\text{em},lj}(\boldsymbol{q})$ is the element from the l's row and the j's column of the emission Jones matrix. Compared with the Eq. (3), the generalized Jones matrix ($\bar{\boldsymbol{M}}_{\text{em},lj}(\boldsymbol{q})$) extends the scalar emission PSF model to vectorial emission PSF model. The mathematics details about the generalized Jones matrix are in the Supplement 1. We considered the freely rotated emission dipole situation such that each polarization contributes to the PSF equally:

$$\text{H}_{\text{em}}(\boldsymbol{u}, u_z) = \frac{1}{3} \sum_{l=x,y} \sum_{j=x,y,z} \left|\text{E}_{\text{em},lj}(\boldsymbol{u}, u_z)\right|^2. \tag{12}$$

2.2.2.   Vectorial excitation PSF

For the excitation path, the electric field should be described as:

$$\text{E}_{\text{ex},lj}(\boldsymbol{u}, u_z) = \frac{1}{\sqrt{2\pi}} \int d^2q\, c_{\text{ex},lj}(\boldsymbol{q}) \exp\left(-i\mathbf{k}_{\text{ex}}(\boldsymbol{q}) \cdot \boldsymbol{u}\right) \exp\left(-ik_z u_z\right),$$

$$c_{\text{ex},lj}(\boldsymbol{q}) = \begin{cases} A_{\text{ex}}(\boldsymbol{q})\, \bar{\boldsymbol{M}}_{\text{ex},lj}(\boldsymbol{q})\, \bar{I}_{\text{ex},j} \exp\left(-i\frac{2\pi W_{\text{ex}}(\boldsymbol{q})}{\lambda_{\text{ex}}}\right) & , |\boldsymbol{q}| \leqslant 1 \\ 0 & , |\boldsymbol{q}| > 1 \end{cases}, \tag{13}$$

with

$$\bar{I}_{\text{ex}} = \begin{bmatrix} I_x e^{i\delta_x} \\ I_y e^{i\delta_y} \end{bmatrix}, \tag{14}$$

where $I_{x,y}$ standards for the amplitude of x, y polarization and $\delta_{x,y}$ standards for the phase delay of x, y polarization, which determines the chirality of excitation light, and where $\bar{M}_{\text{ex},lj}(\boldsymbol{q})$ is the

element from the l's row and the j's column of the excitation Jones matrix, which is detailed defined in the Supplement 1. The excitation light incidents the pupil plane with two polarization directions (x, y), and after the refraction by the objective lens, the excitation light has the fraction on three polarization directions (x, y, z), $\bar{I}_{ex}$ stands for the polarization of excitation light source, and λ_{em} is the wavelength of excitation light.

The PSF of excitation ($H_{ex}(\cdot)$) can be described as

$$H_{ex}(\boldsymbol{u}, u_z) = \sum_{l=x,y,z} \sum_{j=x,y} \left| E_{ex,lj}(\boldsymbol{u}, u_z) \right|^2. \tag{15}$$

2.3. Vectorial theory of multi-photon image scanning microscopy PSF

In the previous ISM theory, the excitation wavelength is considered the same as the emission wavelength, which limits the exploration of multi-photon ISM. To investigate multi-photon ISM, we start from Eq. (7), but the excitation wavelength for 2-photon and 3-photon excitation is twice and three times larger, respectively, than the 1-photon excitation wavelength. The electric field of the k-photon excitation PSF can be described as follows:

$$E_{ex,lj}(\boldsymbol{u}, u_z) = \frac{1}{\sqrt{2\pi}} \int d^2q \, c_{ex,lj}(\boldsymbol{q}) \exp\left(-i\mathbf{k}_{ex}(\boldsymbol{q}) \cdot \boldsymbol{u}\right) \exp\left(-ik_z u_z\right),$$

$$c_{ex,lj}(\boldsymbol{q}) = \begin{cases} A(\boldsymbol{q}) \bar{M}_{lj}(\boldsymbol{q}) \bar{I}_{ex,j} \exp\left(-i\frac{2\pi W_{ex}(\boldsymbol{q})}{\lambda_{ex}}\right) & , |\boldsymbol{q}| \leqslant 1 \\ 0 & , |\boldsymbol{q}| > 1 \end{cases}, \tag{16}$$

where the subscript l stands for l-component of electric field, λ_{ex} is the excitation wavelength of multi-photon excitation. The multi-photon excitation PSF (H_{ex}) can be described as follows:

$$H_{ex}(\boldsymbol{u}, u_z) = \sum_{l=x,y,z} \sum_{j=x,y} \left| E_{ex,lj}(\boldsymbol{u}, u_z) \right|^2. \tag{17}$$

Afterward, the effective multi-photon excitation PSF should consider the photon absorption possibility. The effective multi-photon [23] excitation PSF is:

$$H_{ex,k}(\boldsymbol{u}, u_z) = H_{ex}(\boldsymbol{u}, u_z)^k, \tag{18}$$

where the subscript k stands for k-photons excitation. In the simulation of multi-photon ISM PSF (Eq. (1)) we used the effective multi-photon excitation PSF ($H_{ex,k}$) as the excitation PSF (H_{ex}).

2.4. Computation method for the scalar and vectorial ISM PSF

The method for simulating the ISM PSF involves evaluating the equations described in Sections 2.1 and 2.2. To obtain the optical transfer function (OTF) of the excitation and emission PSFs, the chirp z-transform method is used. This method is commonly employed for fast and accurate computation of discrete Fourier transforms and is well-suited for simulating the PSFs in ISM.

In the simulation, the excitation and emission PSFs are evaluated using a pixel size of 5 nm and a simulation window size of 512 pixels. For simulating the vectorial excitation PSF, circular polarization is chosen as the simulation condition. The excitation wavelength is set to 640 nm for both 1-photon and 2-photon excitation, while for 3-photon excitation, the excitation wavelengths are 1280 nm and 1920 nm, respectively. The emission wavelength is fixed at 690 nm for all simulation scenarios.

The numerical aperture (NA) of the objective lens is specified as 1.35. The refractive index of the coverslip and immersion medium is set to 1.52, while the refractive index of the sample medium is 1.33.

The size of the simulation window at the Fourier plane is determined as 8NA/640 nm, and it is discretized with a total of 201 pixels in both the x and y directions. In the majority of simulations presented in this study, we select a sweep factor (M) of 2 for the ISM PSF to attain optimal resolution. Conversely, a sweep factor of 1 is employed for the Confocal PSF. It is important to note that in the case of the confocal PSF, we refer to the PSF acquired through a camera sensor, rather than a photon detector, as our equation does not involve the summation of photons over the detector area. For the simulation of multi-photon ISM, we vary the sweep factor to explore the optimal FWHM of the PSF.

By following these simulation conditions and using the chirp z-transform method, the scalar and vectorial ISM PSFs can be computed for various excitation scenarios, allowing for the investigation and analysis of multi-photon ISM.

3. Results

3.1. Effects of Stokes shift and polarization on image scanning microscopy PSF

In this section, we investigate the influence of Stokes shift and polarization on the excitation, emission, and PSFs. We compare these PSFs with their scalar counterparts to highlight the impact of vectorial effects in Fig. 1. We consider three scenarios: (1) "vectorial + Stokes shift" where both polarization and Stokes shift are taken into account, (2) "vectorial + no Stokes shift" where only polarization is considered without Stokes shift, and (3) "scalar + no Stokes shift" where neither polarization nor Stokes shift are considered. The optical transfer function (OTF) and PSF are analyzed to compare these scenarios. Additionally, cross-section profiles are presented to visualize the differences between the PSFs.

In Fig. 1(f–h), we show the OTF and PSF with and without the consideration of polarization and the Stokes effect. In Fig. 1(i–k), we show the cross-section of them to visualize the difference. Comparing the cross-section curve from "vectorial + Stokes shift" and "vectorial + no Stokes shift" (Fig. 1(i–k)), we observe that the effect of polarization delivers more difference than Stokes shift. Besides, for a pinhole size of 1.0, the FWHM of the vectorial ISM PSF is 25% larger than the scalar ISM PSF (Fig. 1(k)).The observed phenomenon can be attributed to the interplay of various physical factors within the vectorial model. Notably, the pupil function undergoes additional modulation due to the influence of the Fresnel effect and the projection of the polarization field. These effects collectively introduce an amplitude term into the pupil function, which, in the spatial domain, can be likened to the operation of a Gaussian kernel, resulting in further blurring of the PSF. Consequently, this leads to the empirical observation of a broader PSF. A similar rationale has been proposed in prior research on vectorial PSF, as documented in Hanser's work [15].

3.2. Comparison of scalar and vectorial ISM PSF for resolution improvement

In this section, we examine the impact of polarization on the image scanning microscopy point spread function and assess the resolution improvement achieved by ISM compared to widefield and confocal PSFs. For the widefield PSF, we utilize the emission PSF (H_{em}), while the confocal PSF is obtained by setting the rescan factor to $M = 1$. We refer to the PSF without considering polarization and Stokes shift as the scalar PSF, and the PSF considering polarization and Stokes shift as the vectorial PSF.

Figure 2(a) shows the FWHM of widefield, confocal, and ISM PSF. We found the consideration of the polarization can broaden the FWHM of the PSFs (Fig. 2(a)). We observed that the minimum FWHM of vectorial image scanning PSF is 202 nm and scalar image scanning PSF is 150 nm. Besides, in many different pinhole sizes, the FWHM of vectorial ISM PSFs deviates significantly from scalar ISM PSF. In Fig. 2(b), we show the improvement of ISM PSF over WF PSF. We find that the scalar PSF model underestimates the improvement and that it is slightly
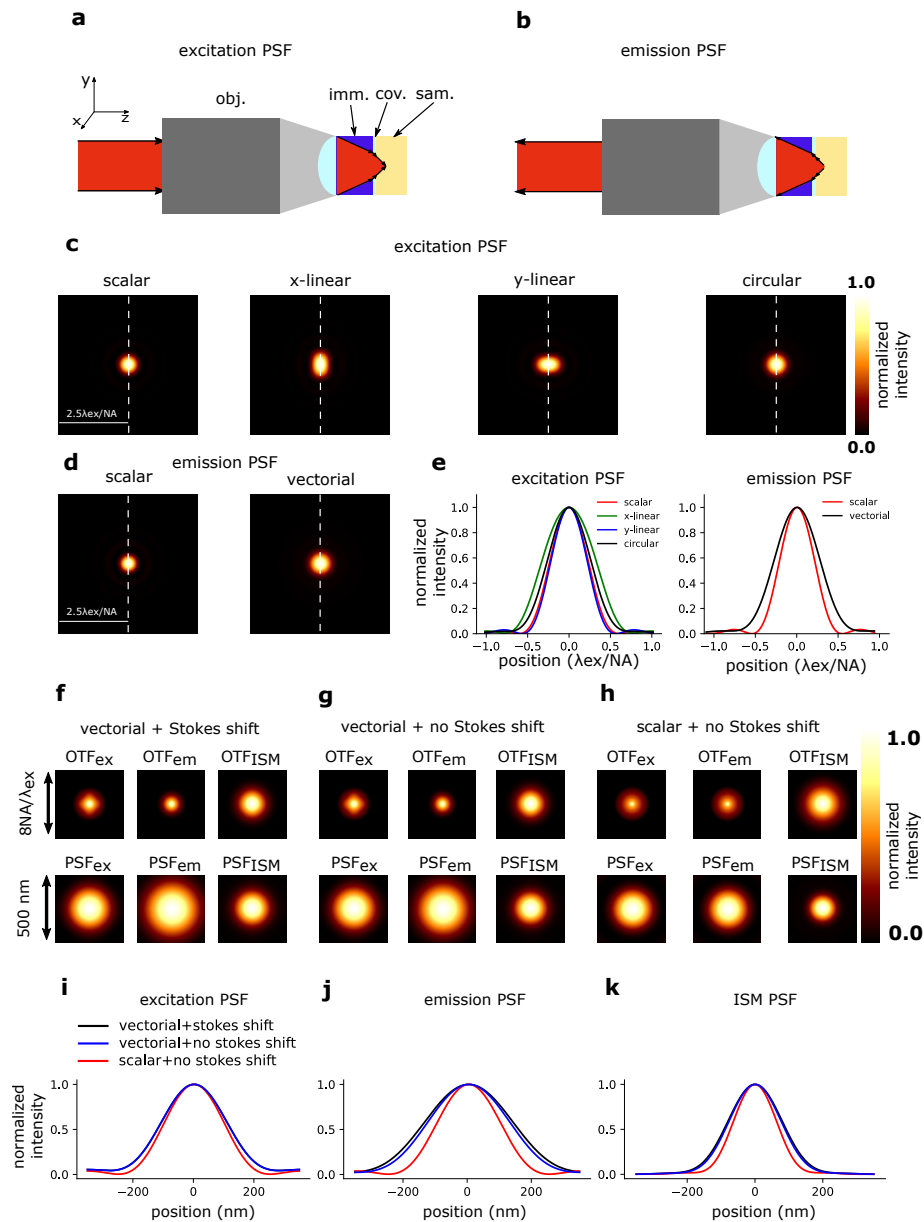
Fig. 1. Demonstrate the difference between the vectorial and scalar PSF model. (a,b) In this paper, we consider the physical environment in that the light of excitation and emission PSF experiences the immersion media, coverslip, and sample media. The refractive index difference between different media refracts light which affects the polarization state. imm., cov., and sam. in panel stands for the immersion media, coverslip, and sample media respectively. The arrow direction identifies the propagation direction of light. (c) The comparison between the scalar and the vectorial PSF. For several different excitation polarizations PSF (x-linear, y-linear, circular). (d) Scalar and vectorial emission PSF. (e) Cross-section of excitation and emission PSF. (f–h) OTF and PSF of excitation, emission, and image scanning with/without the consideration of polarization and Stokes shift. (i–k) Cross-section profile of excitation, emission, and image scanning PSF with and without the consideration of polarization and Stokes shift. vectorial+Stokes shift: with consideration of the effect of polarization and the excitation and emission wavelength are different. vectorial+no Stokes shift: considering the effect of polarization and the excitation and emission wavelength are the same. scalar+no Stokes shift: without considering the polarization and the excitation and emission wavelength are the same.

above the $\sqrt{2}$ for pinhole sizes between zero and two. The maximum improvement is achieved with a pinhole of 1.2 Airy unit (A.U.), which delivers an improvement of 1.46 assuming a scalar PSF and 1.48 assuming a vectorial PSF. In Fig. 2(c), the maximum improvement of ISM PSF over confocal PSF is 1.45 in the vectorial PSF model and 1.46 in the scalar PSF model. In the large pinhole condition (pinhole size>2.0 A.U.), the improvement estimated by the scalar theory can be 1.36, but the one estimated by the vectorial theory is 1.40.

We assess the FWHM of both scalar and vectorial PSF as a function of the sweep factor. Figure 2(d-f) provides a visual representation of these evaluations. Figure 2(e) highlights the critical finding that the optimal sweep factor for the scalar PSF is precisely 2. In contrast, the vectorial PSF model yields an optimal sweep factor of 2.13, a result consistent with the data presented in Fig. 2(f). Expanding our investigation, Fig. 2(g) illustrates the FWHM of the PSF across varying depths. Subsequently, Fig. 2(h-i) reveals distinct behaviors in the improvement factors. Specifically, the improvement factor of the scalar PSF demonstrates a rapid decrease, while the vectorial PSF exhibits a relatively slower decline. These observations suggest intriguing nuances in the performance of the two PSF models.

3.3. Comparison of scalar and vectorial PSF models for different NA

The numerical aperture (NA) of a microscope plays a crucial role in determining the width of the point spread function. Increasing the NA leads to a decrease in the FWHM of the PSF, highlighting the wave and vectorial nature of light. In this section, we investigate the impact of NA on the ISM PSF by simulating it using both scalar and vectorial PSF models. We also evaluate the significance of considering the polarization effect for high NA ISM.

In Fig. 3 (a), we show the FWHM of ISM PSF calculated by scalar and vectorial PSF theory at different NA. To quantify the difference between scalar and vectorial ISM PSF, we defined the difference (ϵ) and difference ratio (R_ϵ) as follows:

$$\epsilon = r_{\mathrm{v}} - r_{\mathrm{s}} \qquad (19)$$

$$R_\epsilon = \frac{\epsilon}{r_{\mathrm{v}}} \qquad (20)$$

where r_{v} is the FWHM of vectorial ISM PSF and r_{s} is the FWHM of scalar ISM PSF.

In Fig. 3(b), we show the difference ratio over different NA. We observe that with increasing NA, the difference ratio increases. When the NA is 1.2, the difference (ϵ) is 45 nm and the different ratio can raise to 30%, which means the size between scalar and vectorial ISM PSF can deviate by 30%. This result suggests that the relative difference increases for all ascending values of the NA. Secondly, the absolute difference also increases from NA>0.6 onwards. Therefore, not only does the difference between the models outlast the FWHM reduction for high NA, but the difference between models grows for high NA despite the total FWHM decreasing. The visualization of the PSFs for both scalar and vectorial ISM simulations is presented in Supplement 1, Fig. S2.

3.4. Image scanning PSF with consideration of aberrations

In previous studies, the image scanning theory assumed a perfect, non-aberrated pupil function [11,18], which is often not satisfied in practical experiments. Aberrations can occur in various parts of the imaging system, including the sample and lenses, and they can significantly affect the resolution of image scanning microscopy. In this section, we investigate the impact of aberrations on the ISM PSF.

To simulate the ISM PSF under the effect of aberrations, we consider aberrations that are simultaneously present in the excitation and emission PSFs, which means the aberration terms W_{ex}, W_{em} in Eqs. (11) and (7) are equal.
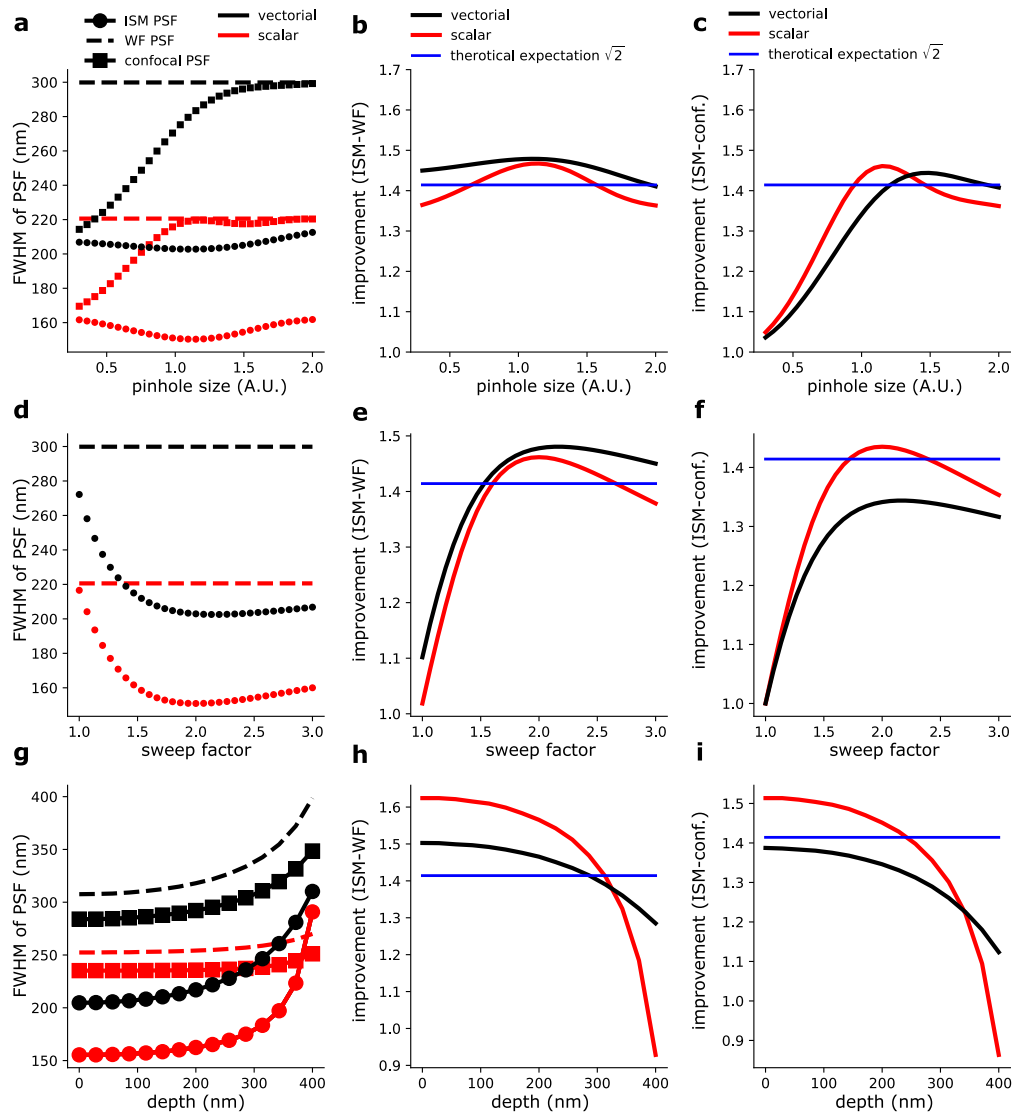
Fig. 2. Comparison of the FWHM and improvement of confocal (conf.) PSF, and image scanning microscopy PSF over the different sizes of pinhole and widefield (WF) PSF. The pinhole does not affect the WF PSF and the FWHM of WF PSF is constant over the different sizes of a pinhole. (a) FWHM of WF, confocal, and ISM PSF with and without the consideration of polarization and Stokes shift. (b) The improvement between ISM and WF PSF with and without consideration of polarization and Stokes shift. (c) The improvement between ISM and confocal PSF with and without consideration of polarization and Stokes shift. (d) FWHM of the PSF for varying sweep factors. (e) Enhancement Factor comparing Image Scanning Microscopy (ISM) and Widefield (WF) PSFs across different sweep factors. (f) Enhancement Factor comparing ISM and Confocal PSFs under varying sweep factors. (g) FWHM of WF, Confocal, and ISM PSFs with and without considering polarization and Stokes shift effects. (h) Improvement Factor for Scalar and Vectorial ISM PSFs over Widefield PSFs at different depths.(i) Improvement Factor for Scalar and Vectorial ISM PSFs over Confocal PSFs at different depths. The sweep factor is set to 2 and the pinhole size is fixed at 1 A.U.
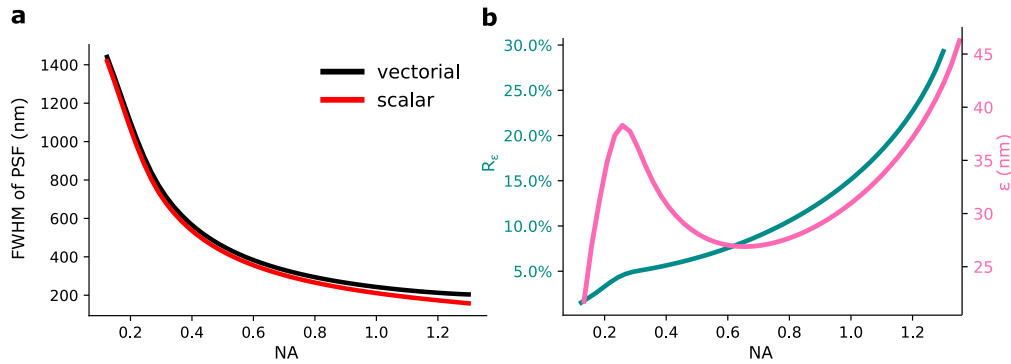
Fig. 3. Benchmark of ISM PSF at different NA calculated by scalar and vectorial PSF theory. In the simulation, the pinhole size is chosen as 1 A.U. (a) The FWHM of PSF at different NA is calculated by scalar and vectorial PSF theory. (b) The difference ratio (R_ϵ) and the difference (ϵ) between scalar and vectorial PSF. The sub-figure shows the R_ϵ ratio at different NA.

We calculated the WF, confocal, and image scanning PSF under different amplitude of aberration (0 mλ, 36 mλ, 72 mλ). The amplitude of aberrations is defined based on the root mean square value of Zernike coefficients, which is computed as $Z_{\text{RMS}} = \sqrt{\sum_{i=1}^{24} C_i^2}$. The C_i stands for the Zernike coefficient of ith Zernike mode following Noll's indexing [26]. The aberrations terms ($W_{\text{ex}}, W_{\text{em}}$) are modeled as the summation of the first 24 Zernike modes after piston, tilt, tip, and defocus modes, since only the latter modes distort the PSF. We randomly assign an aberration to the first 24 Zernike modes. This is achieved by sampling each element from a uniform distribution and subsequently normalizing the vector to achieve the desired aberration strength. In Fig. 4(a), we show the width of PSF at different pinhole sizes and aberrations. In the WF and ISM PSF, we observed that the FWHM of WF, confocal, and ISM PSFs increased as the aberrations increased. This observation aligns with the physical intuition because the aberrations can distort the PSF. However, the effect of aberrations on the confocal PSFs is not as significant as the one in ISM although both of them use pinhole in the emission path (Fig. 4(a)). In Fig. 4(b), we show the improvement of ISM PSF over WF PSF and over confocal PSF under different levels of aberrations. The maximum improvement happens around the 1 A.U. pinhole in all situations we have investigated. With small pinhole sizes (< 1 A.U.), the improvement of ISM over WF and confocal does not reduce a lot by the aberration. However, in large pinholes (> 1 A.U.), the improvement drops down significantly. With 72 mλ aberrations, the improvement between ISM and WF PSF is 1.44 ± 0.033 when the pinhole size is 0.3 A.U. and the improvement is 1.34 ± 0.044 when the pinhole size is 2.0 A.U. The pinhole size should be smaller than 1.5 A.U. and the improvement factor between ISM and confocal PSF can reach the theoretical expectation $\sqrt{2}$.

We conducted simulations of the point spread function (PSF) for WF, confocal, and ISM under strong aberration conditions (Fig. 4(c,d,e)). Under such challenging aberration conditions, the distribution of improvement factors exhibited a notably broader range. This posed a challenge when attempting to ascertain an average improvement in the ISM, particularly in the context of comparing it with the WF imaging. To address this issue, we shifted our focus to assessing whether ISM could still demonstrate improvement under these severe aberration conditions. We defined the possibility of achieving improvement as situations in which the improvement factor exceeded 1, as shown in Fig. 4(e). To ensure a fair and robust quantification of this possibility, we performed 60 simulations for each condition, considering different aberration amplitudes and pinhole sizes (1 A.U. and 2 A.U.).The results, depicted in Fig. 4(e), revealed that when
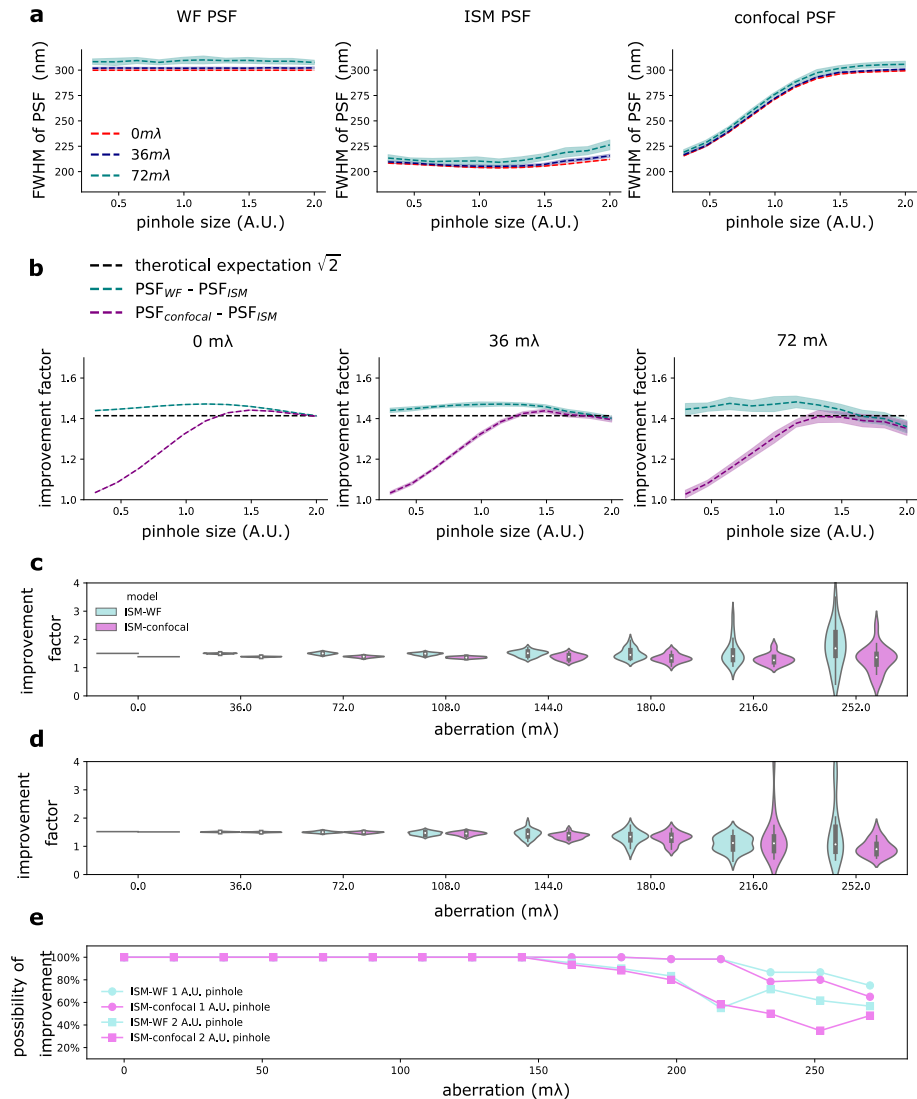
Fig. 4. Benchmark the width of widefield (WF) PSF, image scanning microscopy PSF, and confocal PSF and the improvement. The PSFs in this simulation are all calculated by a vectorial model. (a) The FWHM of WF, ISM, and confocal PSF at a different level of aberration (0 mλ, 36 mλ, 72 mλ) and pinhole size. The aberration of WF, confocal, and image scanning PSF are randomly assigned to 24 Zernike modes. We measured the width of each PSF from 10 different random aberrations. The filled region in each sub-panel is the standard deviation from 20 measurements. (b) Benchmark the improvement of ISM PSF over WF PSF and ISM PSF over confocal PSF. The improvement is defined as $\frac{r_{\text{WF, confocal}}}{r_{\text{ISM}}}$, where $r_{\text{WF, confocal}}$ is the FWHM of widefield and confocal PSF respectively, and r_{ISM} is the FWHM of ISM PSF. (c) The improvement factor of ISM PSF over WF PSF and ISM PSF over confocal PSF in 1 A.U. of the pinhole. (d) The improvement factor of ISM PSF over WF PSF and ISM PSF over confocal PSF in 2 A.U. of pinhole. (e) Feasibility of achieving an improvement. We define 'achieving improvement' as the scenario where the improvement factor exceeds 1.

using a 1 A.U. pinhole, ISM consistently achieved improvement until an aberration amplitude of 216 mλ. In contrast, under the 2 A.U. pinhole condition, ISM maintained its ability to achieve improvement only up to an aberration amplitude of 144 mλ. These findings shed light on the impact of pinhole size and aberration amplitude on the ISM technique's capability to enhance imaging quality under challenging aberration conditions.

3.5. Multi-photon excitation in image scanning microscopy

When imaging thick samples, multi-photon excitation is commonly employed to minimize scattering induced by the sample. The longer wavelength used in multi-photon excitation reduces scattering effects, but it also increases the FWHM of the PSF. Additionally, the nonlinear absorbance of the light in multi-photon excitation virtually narrows the excitation PSF, resulting in what is known as the effective excitation PSF. In this section, we use the vectorial PSF theory to investigate 2-photon and 3-photon excitation in image scanning microscopy.

In Fig. 5(a), we show the excitation PSF (H_{ex}), effective excitation PSF ($H_{ex,eff}$), and ISM PSF (H_{ISM}) with 1,2,3-photon excitation. The excitation PSF of multiple photon excitation is wider as the excitation wavelength is longer. In ISM PSF simulation, we care more about the effective excitation PSF since that is the one we used for ISM PSF simulation. In Fig. 5(b), we show the cross-section of effective excitation PSF with 1,2,3-photon excitation. We observe that the FWHM of multiple photon effective excitation PSFs is larger. The physics behind this can be explained as follows. We can model the excitation PSF with a simple Gaussian function.

$$H_{ex} \sim e^{-\frac{r^2}{2\sigma^2}}, \tag{21}$$

where r is the distance from the center of PSF and σ is the standard deviation of the PSF. The standard deviation σ is proportional to the wavelength and NA through the diffraction limit:

$$\sigma \propto \frac{\lambda}{2\text{NA}}. \tag{22}$$

For k-photon excitation, the excitation wavelength is k times larger than the one of 1-photon excitation wavelength, and hence the width of k-photon excitation PSF (σ_k) can be expressed as:

$$\sigma_k \propto \frac{\lambda_k}{2\text{NA}} = \frac{k\lambda_1}{2\text{NA}} \propto k\sigma_1, \tag{23}$$

where σ_1 and σ_k is the width of 1-photon and k-photon excitation PSF and λ_1 and λ_k is the wavelength of 1-photon and k-photon excitation wavelength. The effective k-photon excitation PSF can be expressed as:

$$H_{ex,k}(r) \propto e^{-\frac{r^2}{2k\sigma_1^2}}. \tag{24}$$

In Fig. 5(c), we present an analysis of the FWHM for the PSF of single/multi-photon excitation in ISM. Our findings reveal that a sweep factor of 2 may not always be the ideal choice for multiple-photon excitation ISM. Interestingly, we have identified distinct optimal sweep factors for different excitation modalities. Specifically, for 2-photon excitation ISM, the optimal sweep factor is determined to be 1.53, whereas for 3-photon excitation ISM, the optimal sweep factor is 1.4. Notably, a sweep factor of 2 is found to be optimal for one-photon excitation ISM (as illustrated in Fig. 5(c)).

In Fig. 5(e), we show the FWHM of one-photon/multi-photon excitation ISM PSF with a sweep factor of 2 or with an optimal sweep factor. We found that the FWHM of the ISM PSF is larger for multi-photon excitation than 1-photon excitation. This is because the FWHM of the effective excitation PSF ($H_{k,ex}$) of multi-photon ISM is larger than the 1-photon excitation ISM, and this, in turn, broadens the multi-photon excitation ISM PSF. When the pinhole size is
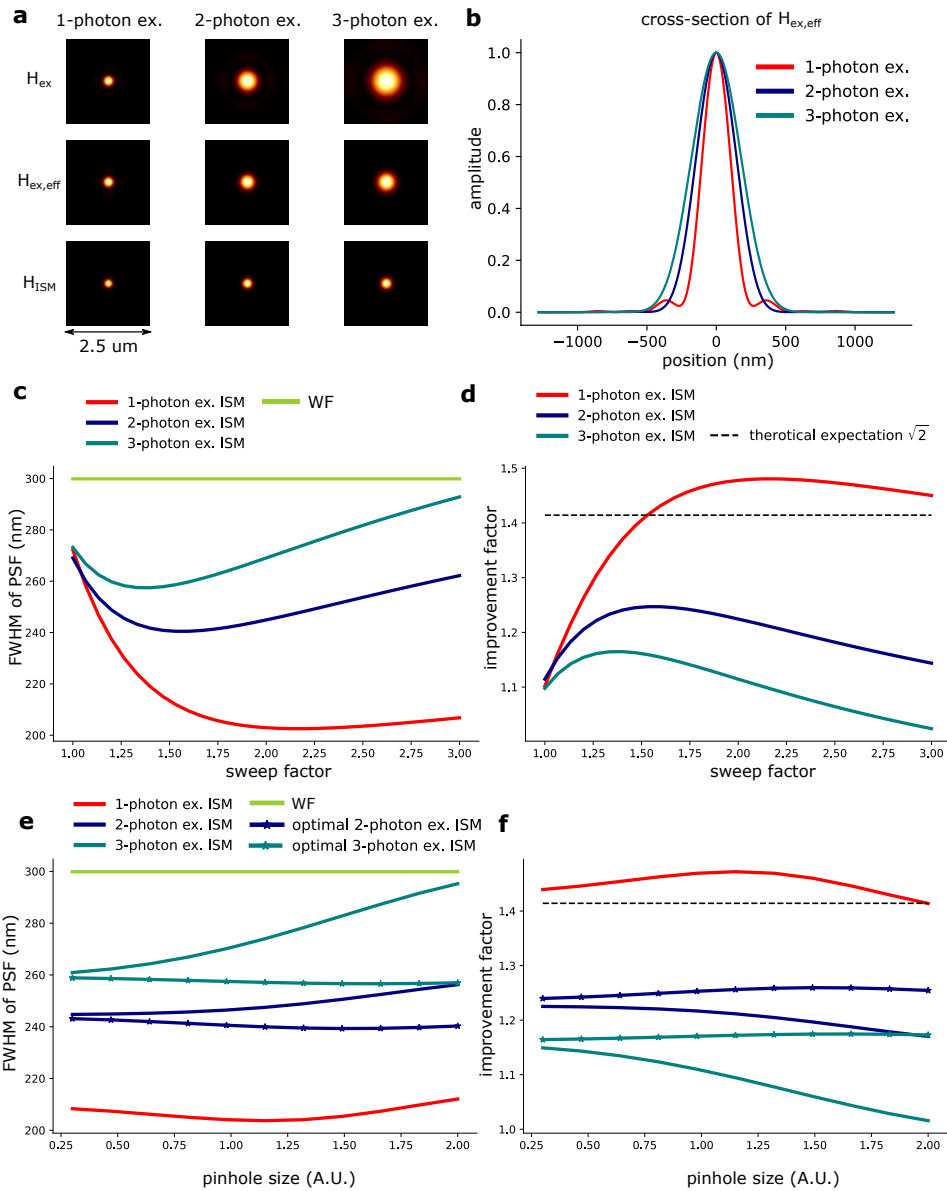
Fig. 5. The width of multi-photon excitation ISM PSF and the improvement. (a) The excitation PSF (H_{ex}), effective excitation PSF ($H_{ex,eff}$), and ISM PSF under 1,2,3-photon excitation. The abbreviation ex. stands for excitation. The white dashed lines indicate the cross-section of the panel (b). (b) The cross-section profile of effective excitation PSF from 1,2,3-photon excitation. (c) The FWHM of 1,2,3-photon excitation ISM and widefield(WF) PSF under different sweep factors. The sweep factor does not affect widefield PSF. It is shown for reference. (d) Improvement of single and multi-photon ISM PSF over widefield PSF under different sweep factors. (e) The FWHM of PSF of multi-photon ISM under different pinhole sizes. The solid line stands for the ISM PSF simulated with a sweep factor of 2 and the dotted line stands for the ISM simulated with an optimal sweep factor searched by the data from sub-panel (c). In 2-photon excitation ISM PSF, the optimal sweep factor is 1.533 and in 3-photon excitation ISM PSF the optimal sweep factor is 1.4. (f) Improvement of single and multi-photon ISM PSF over widefield PSF under different pinhole sizes. For (c,d), the A.U. is defined as $\frac{1.22\lambda_{ex}}{NA}$, where λ_{ex} is 640 nm.

1 A.U., the FWHM of 1-photon excitation ISM PSF is 189 nm, 2-photon excitation ISM PSF is 244 nm, and 3-photon excitation ISM PSF is 268 nm, which stands for a 20% increment of FWHM of 2-photon excitation ISM PSF and a 28% increment of FWHM of 3-photon excitation ISM PSF comparing with the 1-photon excitation ISM. In Fig. 5(d), we show the improvement of multi-photon ISM over widefield. With the multi-photon excitation, the improvement of ISM over WF decreases. Under the simulation we have investigated, the maximum improvement of 1-photon excitation ISM is 1.47, 2-photon excitation ISM is 1.22, and 3-photon excitation ISM is 1.12. In all calculated situations, the improvement of two and 3-photon excitation cannot be higher than the theoretical expectation $\sqrt{2}$. We also conducted simulations of the multi-photon ISM PSF using the optimal sweep factors, which were determined to be 1.53 for 2-photon ISM and 1.4 for 3-photon ISM. It is worth noting that the optimal sweep factor, as illustrated in Fig. 5(c), was identified under the specific condition of a 1 A.U. pinhole aperture. Importantly, our results consistently demonstrate that employing the optimal sweep factors consistently yields a narrower FWHM compared to using a sweep factor of 2 across various pinhole conditions. Under the specific condition of a 1 A.U. pinhole, our simulations revealed that the FWHM for 2-photon excitation ISM using the optimal sweep factor was 240 nm, whereas the FWHM for 2-photon excitation ISM with a sweep factor of 2 was slightly larger at 244 nm. In the case of 3-photon excitation ISM, the FWHM of the PSF with the optimal sweep factor was 257 nm, while the FWHM of the PSF with a sweep factor of 2 measured a larger value of 268 nm. These findings underscore the significance of the optimal sweep factor in achieving superior PSF performance in ISM applications.

4.   Conclusion

In this paper, we have developed a vectorial theory of ISM by taking into account aberration, polarization, and Stokes shifts between excitation and emission. Previous ISM research predominantly relied on scalar theory, neglecting the high-NA effects that are present. To illustrate the disparity between scalar and vectorial ISM PSF models, we present the OTF and PSF in Fig. 1. The vectorial ISM PSF exhibits a FWHM that is 25% larger than the scalar ISM PSF, signifying a significant distinction. This disparity primarily arises from the effect of polarization rather than the Stokes shifts.

To further validate the advantages of employing vectorial theory in ISM PSF simulation, we conduct a benchmark by comparing the FWHM of the WF, confocal, and ISM PSF calculated based on both scalar and vectorial PSF theories. In our simulation, we observe that the FWHM of vectorial ISM PSFs is approximately 54 nm larger than those estimated by the scalar ISM PSF theory when the pinhole size is set to 1 A.U. (Fig. 2(a)). Figure 2(b,c) suggests that the scalar theory and theoretical expectations slightly underestimate the resolution improvement offered by ISM in comparison to the estimates provided by the vectorial theory. In the benchmark between WF and ISM, the maximum improvement predicted by the vectorial ISM model can reach up to 1.48 when the pinhole size is set to 1.1 A.U. Similarly, in the benchmark between confocal and ISM, the improvement predicted by the vectorial ISM model can reach up to 1.46 when the pinhole size is set to 1.49 A.U. In addition, the scalar ISM PSF demonstrates an optimal sweep factor prediction of 2, while the vectorial ISM PSF predicts a slightly higher value of 2.13 (as depicted in Fig. 2(e,f)). It is worth noting that the depth of imaging has a significant impact on the ISM PSF's performance, with the improvement factor diminishing as imaging depth increases (as shown in Fig. 2(h,i)). Interestingly, the scalar ISM PSF exhibits a more pronounced decline in the improvement factor across various imaging depths compared to the vectorial ISM PSF (as illustrated in Fig. 2(h,i)).

To further reinforce the rationale behind employing vectorial theory in ISM PSF simulation, we compare the ISM PSF calculated using scalar and vectorial theories at different NA (Fig. 3). The results indicate that the difference ratio (R_ϵ) between scalar and vectorial ISM PSF can

increase up to 30% when NA is 1.3, while the difference ratio is only 5% when the NA is 0.1. This emphasizes the significance of considering polarization effects, particularly in high NA ISM PSF simulations. Based on the comparisons made between the scalar and vectorial ISM PSF models (Fig. 2 and Fig. 3), we conclude that both models can accurately predict the resolution improvement of ISM, but the scalar PSF model tends to underestimate the FWHM of the PSF when compared to the estimates provided by the vectorial PSF model.

Additionally, we investigate the influence of aberration and pinhole size on the ISM PSF. In Fig. 4, we demonstrate that aberration broadens the ISM PSF, leading to a deterioration in resolution and affecting the overall improvement. In the case of a 72 mλ situation, which is usually considered a diffraction limit condition, ISM with a 0.3 A.U. pinhole achieves an improvement of 1.45 ± 0.022, whereas using a 2.0 A.U. pinhole only yields an improvement of 1.35 ± 0.038. This qualitative outcome suggests that employing a smaller pinhole can counteract the deterioration of the PSF caused by aberrations when compared to using a larger pinhole. However, it's worth noting that a smaller pinhole rejects more emission signals, resulting in poorer imaging quality. In addition, we conducted simulations of WF, confocal, and ISM PSF under high aberration conditions, reaching up to 252 mλ. Our investigation revealed that reducing the pinhole size can significantly improve ISM's performance in the presence of high aberrations. Specifically, with a pinhole size of 1 A.U., ISM consistently exhibited improvements until the aberration reached 216 mλ. However, when using a 2 A.U. pinhole, ISM's performance started to deteriorate for aberrations exceeding 144 mλ. This observation is illustrated in Fig. 4.

Additionally, we explored the potential of leveraging multi-photon excitation in ISM and compared the ISM PSFs generated by 1-photon and multi-photon excitation. Our qualitative assessment indicated that multi-photon ISM PSFs are wider than their 1-photon counterparts, primarily due to the broader multi-photon excitation PSF. This broader excitation PSF ultimately results in a broader ISM PSF, as shown in Fig. 5(a). Notably, the optimal sweep factor for multi-photon ISM is not 2 but rather 1.53 for 2-photon excitation ISM and 1.4 for 3-photon excitation ISM (Fig. 5(c,d)), all of which were observed when using a 1 A.U. pinhole.

This trend in the optimal sweep factor can be attributed to the effective excitation PSF's width in multi-photon ISM, which is wider than in 1-photon excitation ISM. Furthermore, the OTF of the excitation PSF is narrower compared to that of the one-photon excitation PSF. According to Eq. (2), a narrower OTF constrains the range of usable sweep factors in ISM. Exceeding this range can shift the excitation OTF outside the emission OTF, resulting in an ineffective expansion of the effective OTF.

In the comparison between ISM and WF PSFs, our results consistently demonstrated that the optimal sweep factor always produced a narrower ISM PSF, regardless of the pinhole size (Fig. 5(e)). However, multi-photon ISM fell short of achieving the theoretical expectation of $\sqrt{2}$ improvement, even with the optimal sweep factor. The maximum improvement we observed was 1.22 for 2-photon excitation ISM, 1.25 for 2-photon excitation ISM with the optimal sweep factor, 1.15 for 3-photon excitation ISM, and 1.17 for 3-photon excitation ISM with the optimal sweep factor (Fig. 5 (f)). Notably, the influence of the optimal sweep factor on ISM PSF was weaker when a smaller pinhole was employed, as indicated in Fig. 5 (e,f). This can be attributed to the fact that, when a near-zero pinhole is used in the ISM system, the ISM PSFs become independent of the sweep factor [11], and consequently, the effect of the sweep factor is diminished.

In summary, our findings suggest that optimizing the pinhole size and sweep factor is critical in enhancing ISM performance, particularly in the presence of high aberrations. Additionally, while multi-photon excitation widens the ISM PSF, the choice of optimal sweep factor remains crucial in obtaining the best achievable resolution.

Disclosures. The authors declare no conflicts of interest.

Data availability. The code is freely available at the link found at [27] below.

Supplemental document. See Supplement 1 for supporting content.

References

1. M. Born and E. Wolf, *Principles of optics. Electromagnetic theory of propagation, interference and diffraction of light. 6.* (Pergamon Xxviii, 1993).
2. K. I. Willig, B. Harke, R. Medda, *et al.*, "Sted microscopy with continuous wave beams," Nat. Methods **4**(11), 915–918 (2007).
3. G. Vicidomini, P. Bianchini, and A. Diaspro, "Sted super-resolved microscopy," Nat. Methods **15**(3), 173–182 (2018).
4. M. J. Rust, M. Bates, and X. Zhuang, "Sub-diffraction-limit imaging by stochastic optical reconstruction microscopy (storm)," Nat. Methods **3**(10), 793–796 (2006).
5. E. Betzig, G. H. Patterson, R. Sougrat, *et al.*, "Imaging intracellular fluorescent proteins at nanometer resolution," Science **313**(5793), 1642–1645 (2006).
6. S. T. Hess, T. P. Girirajan, and M. D. Mason, "Ultra-high resolution imaging by fluorescence photoactivation localization microscopy," Biophys. J. **91**(11), 4258–4272 (2006).
7. M. G. L. Gustafsson, "Surpassing the lateral resolution limit by a factor of two using structured illumination microscopy," J. Microsc. **198**(2), 82–87 (2000).
8. C. S. Smith, J. A. Slotman, L. Schermelleh, *et al.*, "Structured illumination microscopy with noise-controlled image reconstructions," Nat. Methods **18**(7), 821–828 (2021).
9. C. J. R. Sheppard, "Super-resolution in confocal imaging," Super-resolution in confocal imaging **80**, 53–54 (1988).
10. S. Roth, C. J. Sheppard, K. Wicker, *et al.*, "Optical photon reassignment microscopy (opra)," Opt. Nano **2**(1), 5 (2013).
11. G. M. D. Luca, R. M. Breedijk, R. A. Brandt, *et al.*, "Re-scan confocal microscopy: scanning twice for better resolution," Biomed. Opt. Express **4**(11), 2644–2656 (2013).
12. C. B. Müller and J. Enderlein, "Image scanning microscopy," Phys. Rev. Lett. **104**(19), 198101 (2010).
13. T. Azuma and T. Kei, "Super-resolution spinning-disk confocal microscopy using optical photon reassignment," Opt. Express **23**(11), 15003–15011 (2015).
14. A. York, P. Chandris, D. D. Nogare, *et al.*, "Instant super-resolution imaging in live cells and embryos via analog image processing," Nat. Methods **10**(11), 1122–1126 (2013).
15. B. M. Hanser, M. G. L. Gustafsson, D. A. Agard, *et al.*, "Phase-retrieved pupil functions in wide-field fluorescence microscopy," J. Microsc. **216**(1), 32–48 (2004).
16. J. J. Braat, P. Dirksen, A. J. Janssen, *et al.*, "Extended nijboer–zernike approach to aberration and birefringence retrieval in a high-numerical-aperture optical system," J. Opt. Soc. Am. A **22**(12), 2635–2650 (2005).
17. M. Siemons, C. N. Hulleman, R. Ø. Thorsen, *et al.*, "High precision wavefront control in point spread function engineering for single emitter localization," Opt. Express **26**(7), 8397–8416 (2018).
18. O. Schulz, C. Pieper, M. Clever, *et al.*, "Resolution doubling in fluorescence microscopy with confocal spinning-disk image scanning microscopy," Proc. Natl. Acad. Sci. **110**(52), 21000–21005 (2013).
19. C. J. R. Sheppard, S. B. Mehta, and R. Heintzmann, "Superresolution by image scanning microscopy using pixel reassignment," Opt. Lett. **38**(15), 2889–2892 (2013).
20. W. Wang, B. Zhang, B. Wu, *et al.*, "Image scanning microscopy with a long depth of focus generated by an annular radially polarized beam," Opt. Express **28**(26), 39288–39298 (2020).
21. I. Gregor, M. Spiecker, R. Petrovsky, *et al.*, "Rapid nonlinear image scanning microscopy," Nat. Methods **14**(11), 1087–1089 (2017).
22. O. Tzang, D. Feldkhun, A. Agrawal, *et al.*, "Two-photon psf-engineered image scanning microscopy," Opt. Lett. **44**(4), 895 (2019).
23. S. V. Koho, E. Slenders, G. Tortarolo, *et al.*, "Two-photon image-scanning microscopy with spad array and blind image reconstruction," Biomed. Opt. Express **11**(6), 2905 (2020).
24. C. J. R. Sheppard, M. Castello, G. Tortarolo, *et al.*, "Image scanning microscopy with multiphoton excitation or bessel beam illumination," J. Opt. Soc. Am. A **37**(10), 1639 (2020).
25. M. E. Siemons, L. C. Kapitein, and S. Stallinga, "Axial accuracy in localization microscopy with 3d point spread function engineering," Opt. Express **30**(16), 28290–28300 (2022).
26. R. J. Noll, "Zernike polynomials and atmospheric turbulence*," J. Opt. Soc. Am. **66**(3), 207–211 (1976).
27. S.T. Hung, D. Kalisvaart, and C. Smith, "ISM-PSF," Github (2023) https://github.com/qnano/ISM-PSF.